Residual alignment and its effect on weld strength in material-extrusion 3D-printing of polylactic acid

Andrea Costanzo[1], Roberto Spotorno[1], María Virginia Candal[2,3], María Mercedes Fernández[2], Alejandro J. Müller[2,4], Richard Graham[5], Dario Cavallo[1] & Claire McIlroy[6]

[1] *Department of Chemistry and Industrial Chemistry, University of Genoa, Genova, Italy, 16146*
[2] *POLYMAT and Polymer Science and Technology Department, Faculty of Chemistry, University of the Basque Country UPV/EHU, Paseo Manuel de Lardizábal, 3, 20018 Donostia-San Sebastián, Spain*
[3] *Universidad Simón Bolívar, Departamento de Mecánica, Grupo de Polímeros, Apartado 89000, Caracas 1080-A, Venezuela*
[4] *IKERBASQUE, Basque Foundation for Science, Bilbao, Spain*
[5] *School of Mathematical Sciences, University of Nottingham, Nottingham, UK, NG7 2QL*
[6] *School of Mathematics & Physics, University of Lincoln, Lincoln, UK, LN6 7TS*

Abstract

Gaining a molecular understanding of material extrusion (MatEx) 3D printing is crucial to predicting and controlling part properties. Here we report the direct observation of distinct birefringence localised to the weld regions between the printed filaments, indicating the presence of molecular orientation that is absent from the bulk of the filament. The value of birefringence at the weld increases at higher prints speeds and lower nozzle temperatures, and is found to be detrimental to the weld strength measured by tensile testing perpendicular to the print direction. We employ a molecularly-aware non-isothermal model of the MatEx flow and cooling process to predict the degree of alignment trapped in the weld at the glass transition. We find that the predicted residual alignment factor, $\bar{A}$, is linearly related to the extent of birefringence, Δn. Thus, by combining experiments and molecular modelling, we show that weld strength is not limited by inter-diffusion, as commonly expected, but instead by the configuration of the entangled polymer network. We adapt the classic molecular interpretation of glassy polymer fracture to explain how the measured weld strength decreases with increasing print speed and decreasing nozzle temperature.

Keywords:
Material Extrusion, Birefringence, Molecular Orientation, Weld Strength, Polylactic acid

1. Introduction

Due to low material and energy requirements, 3D printing of thermoplastics via extrusion-based methods, known as MatEx, is the most economical additive manufacturing technique [1], offering mass customization across a wide range of fields [2, 3, 4, 5]. However, it is clear that further research and advancements in 3D printing technology should be supported for its potential to be realised [6, 7]. Whilst 'rules-of-thumb' for tweaking the print conditions are often employed by users to overcome frequently occurring problems - in particular poor adhesion between deposited filaments - technological advancement will only occur through a fundamental understanding of the process. Often mechanical strength is a key quality factor, thus we must consider the role of molecular structure throughout printing.

Particular attention is given to the non-isothermal welding process at filament-filament interfaces, since the weld line is found to be much weaker than the bulk material [8]. The tear strength of a single weld is governed by the time available for inter-diffusion, which can be obtained from the deposited filament thermal history and polymer rheol-ogy. It is speculated that the observed de-bonding of the welds between filaments in MatEx is due to an anisotropic diffusion mechanism [9]. Furthermore, recent modelling efforts suggest that residual alignment may become locked into the weld region at the glass transition under typical MatEX conditions [10]. However, there is currently no direct experimental evidence of this effect, and how residual anisotropy varies with print conditions is unexplored.

It is well known in traditional polymer processing that molecular anisotropy can lead to weaknesses in plastic parts. Generally, a decrease in fracture toughness with increasing polymer orientation in glassy polymers has been measured for a range of specimen geometries and loading conditions [11, 12, 13]. Since strength of glassy polymers is directly related to the number of entanglements that constrain chains across the fracture plane [14], Embery *et al.* proposed that chain orientation leads to partial disentanglement of the network, which consequently reduces mechanical resistance [15]. More relevant to welding in MatEx, recent molecular dynamics simulations of inter-diffusion following a quenched shear flow show how residual alignment leads to a decrease in the yield stress within

the weld region [16].

In this paper, we observe experimentally for the first time residual alignment trapped into a single-filament wall. Furthermore, this residual alignment is found to be localized only at filament-filament interfaces (welds). Residual alignment is quantified for varying nozzle temperature and print speed using the molecularly-aware model of McIlroy *et al.* [17, 10]. By combining these model results with experimental measurements of the weld toughness, we confirm that reduced weld strength is due to orientation of the polymer molecules that occurs during flow through the nozzle and deposition onto the build plate, rather than poor inter-diffusion. Furthermore, residual alignment pertains to a partially entangled network [18] and thus can be directly correlated to weld toughness [10], in close agreement with the experimental data.

2. Experimental Methods

2.1. Material Properties

The material used in this study is poly (L-lactide) (PLA), indicated with the commercial name 4043D, and with a content of D-isomer of about 4%. The material was purchased both in the form of pellets and as a spool of 1.75 mm filament for MatEx. As shown by the calorimetric analysis displayed in the supporting information, this material has a glass transition temperature, T_g of about 60 °C and a melting temperature of ca. 151 °C. We note that upon standard cooling at a rate of 10 °C/min, the material can barely crystallize and is almost totally amorphous, with a crystallinity index less than 1% (see Appendix A).

The molar mass distribution was measured by means of Size Exclusion Chromatography (SEC), using a Waters 717 autosampler with a differential refractometer (Waters 2410), a pump (LC-20A Shimadzu) and three Waters Styragel columns (HR2, HR4 and HR6). Tetrahydrofuran (THF) was used as a solvent at a flow rate of 1 mL/min and a temperature of 35 °C. The calibration was made employing polystyrene narrow standards (ranging from 580 to 395×10^3 g/mol) to obtain a primary calibration curve. The values obtained are $M_n = 79$ kg/mol and $M_w = 173$ kg/mol for the number and weight average respectively.

PLA's rheological properties were measured with a strain-controlled rotational rheometer (ARES-G2, TA instruments). Before carrying out rheological tests, the PLA is dried overnight in a dehumidifier at 80 °C to remove moisture.

The PLA disks (of approximately 1mm thickness) suitable for rheological measurement have been previously be obtained by lab-scale injection molding of pellet samples. The experiments were carried out under a nitrogen flow and with parallel plate geometry, using plates with a diameter of 25 mm. A rheological master curve was obtained by measuring the elastic modulus, G', and loss modulus, G", as a function of frequency, ω, in the linear viscoelastic regime at different temperatures. The time-temperature superposition (TTS) principle was used to shift frequency

data into a master curve at a reference temperature of 200°C, using a horizontal shift factor that depends on temperature following a Williams-Landel Ferry (WLF) equation. The oscillatory stress was measured in a frequency range from 0.5 to 3×10^5 rad/s, in a deformation range of 1-4 %, at temperatures between 110 °C and 200 °C.

2.2. MatEx Printing

The specimen for testing the weld strength and residual orientation were prepared by means of an Intamsys Funmat HT 3D printer, equipped with a nozzle of 0.4 mm diameter. To protect the PLA feedstock from the effects of humidity, each set of specimens is printed from a new reel of PLA (not previously dried) and kept in a closed chamber prior to printing. To simplify as much as possible the preparation of the samples in view of the subsequent measurements, the chosen printed geometry, similar to that in [19], is that of a free-standing square tube (4 cm $\times$ 4 cm $\times$ 4 cm in size) consisting of a single-filament stack with layer height of 0.4 mm. This means that, within each layer, the nozzle moves along a square path and extrudes a single polymer filament. The sample with the described geometry was designed with the software Tinkercad and subsequently converted into an STL format file for printing. The software Cura was used to generate G-code and to optimize the process conditions.Specimens were printed exploring different processing conditions, namely by varying nozzle temperature and print speed, while keeping the bed and chamber temperatures constant at 60 °C and 35 °C, respectively.

Table 1: Print conditions and geometry.

Parameter	Notation	Value
Nozzle temperature	T_N	$190 - 240$ °C
Bed temperature	T_a	60 °C
Print speed	U_P	5-120 mm s^{-1}
Nozzle radius	R_N	0.2 mm
Layer height	H	0.4 mm
Filament width	W	0.4 mm

2.3. Tensile Testing for Weld Strength

Specimens were subjected to a tensile test (ASTMD1938) to determine weld strength as a function of printing conditions. The printed shapes (square tubes) were first cut along the four side walls using a scissor. Then, three rectangular shape tensile specimens for each print condition were punched out from each side wall with a pneumatic press, with the layer deposition direction oriented at an angle of 90° with respect to the cutting direction. The tested samples have the following dimensions: 40 mm of height, 13 mm of width and roughly 0.45 mm thickness. Rectangular-shaped (single-filament wall) specimens are chosen, rather than a traditional dog-bone shape, due to geometrical constraints imposed by the print size and the

available blade to cut (punch-out) the sample. Furthermore, in this way the strength at the weld between filaments can be isolated from other effects and the measurement can be compared easily to the model.

Additional samples were obtained by placing the walls with the printing direction parallel to that of the pneumatic cutting press. These latter samples should exhibit a tensile strength comparable to the intrinsic PLA bulk strength, i.e. not affected by the welding process occurring during MatEx. We find that this bulk strength measurement yields approximately 52 MPa across all tested print speeds and temperatures. This is in line with values reported in the literature [20], which reports bulk strength values between about 47 and 59 MPa. Tensile tests were carried out using an Instron 5565 S/NO H1505, with an initial distance between the clamps of 12 mm and a separation speed of 6 mm/min.

To derive the tensile strength the actual cross-section of the specimen must be known; for our test geometry derived from 3D-printed walls, this is the weld-area, i.e. the interface between two adjacent printed filaments. While one of the weld widths is considered equal to sample's width (13 mm), the weld-length of such cross-section has been measured using a stereoscope. For each printing condition, three specimens were observed with a Leica stereomicroscope, using a OptikalB5 Digital Camera to capture images of the weld-line. An example micrograph can be found in Appendix B. The exact weld-length was obtained via image analysis with ImageJ software, after calibration with standard microscope ruler. An average of at least 5 measurements was computed for each sample.

The weld strength of the tested sample is calculated as the maximum stress (stress at break) of the tensile stress-strain curve. A representative stress-strain curve is shown in Appendix B. The PLA samples always showed brittle failure exactly along one of the welding lines, at a random distance from the clamped ends. As such, the measured stress at break is considered representative of the actual weld strength of printed specimen.

2.4. Birefringence Measurements

The polymer chain orientation in the printed samples was determined by measuring the birefringence. The measurements were made using a polarized light optical microscope Reichert 350241, coupled with an Ehringaus compensator. Single printed walls were positioned on the rotating object plate, under crossed polarizers condition. The sample was rotated until the printing direction (which coincides with the optical axis of the birefringent printed walls) reached an orientation of 45° with respect to the polarizer transmission directions. In order to measure the birefringence of the sample, the Ehringaus compensator was inserted in the optical path, and rotated around its optical axis until the extinction of the light transmitted by the printed object was achieved. Thanks to the known relation between the compensator crystal's rotation angle and its optical retardation (ϕ), the unknown birefringence
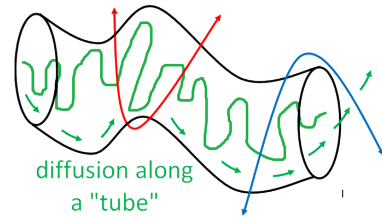

Figure 1: A hypothetical tube region represents constraints due to entanglements. The polymer chain must diffuse (reptate) along the tube to relax.

of the sample (Δn) with a thickness d, can be determined according to $\Delta n = \phi/d$. We note that in the case of the printed walls, the total thickness, measured with digital micrometer, has been used. Since this value does not generally correspond to the actual thickness of the oriented (and birefringent) region, it is more correct to indicate the reported values as 'apparent birefringence'.

3. Numerical Model

The numerical model has been previously developed and employed elsewhere [17, 10, 21, 22]. Thus, here we provide only a brief overview of the model and the governing equations. Further details of the flow modelling is given in Appendix E. In this work, the temperature model has been adapted to account for the dependence of the cooling rate on the print speed, as detailed in Sec.3.3

3.1. Overview

In summary, the model assumes isothermal steady-state flow through an axisymmetric nozzle of radius R_N at some extrusion speed U_N and uniform nozzle temperature T_N. Flow through the nozzle is followed by fast deposition onto a build plate, moving at transverse speed U_P, into an elliptically-shaped filament of thickness H, and width W. The extrusion and transverse print speeds are related to the filament geometry through conservation of mass via

$$\pi R^2 U_N = \frac{\pi}{4} H W U_P. \tag{1}$$

The temperature is assumed to remain uniform during deposition, and is therefore independent of print speed during flow.

The model is molecularly-aware in the sense that polymer stresses are suitably accounted for via a constitutive model (single-mode Rolie-Poly [24]) that considers both the stretching and orientation of the polymer molecules within an entangled network. Entanglements due to neighbouring polymer molecules are represented by a hypothetical tube region [25], which restricts the diffusive motion of a polymer chain to along the tube's contour length (Fig.1). Thus, there are two characteristic time scales to consider:

1. the reptation time τ_d, which is the time taken for the polymer to diffuse along the tube contour length and

Table 2: Model parameters for polylactic acid. Acronyms as follows: TTS = time-temperature superposition, LVE=linear viscoelasticity, GPC=gel permeation chromotography.

Parameter	Notation	Value	Method
WLF parameters	C_1	2.88 °C^{-1}	TTS
	C_2	133.10 °C	TTS
	T_0	200 °C	TTS
Plateau modulus	G_e	4.44×10^5 Pa	LVE model
Entanglement molecular weight	M_e	9.0 kg mol^{-1}	LVE model
Entanglement time (at T_0)	τ_e^0	2.0×10^{-6} s	LVE model
Entanglement number	Z	19	GPC + LVE model
Polydispersity	p	2.2	GPC
Thermal diffusivity	α	5.8×10^{-8} mm^{2}s^{-1}	Ref.[23]

governs the time taken for chain orientation/alignment to relax,

2. the Rouse time τ_R, which is the time taken for the polymer chain to relax within the tube region and governs stretch relaxation.

Explicit formula are given for τ_d and τ_R in the next section. For typical nozzle geometries, print conditions and print materials, the residence time in the nozzle is found to be similar to the polymer reptation time [17]; hence the assumption of steady flow in the nozzle (see Appendix E for further details).

The melt is typically characterised by a dimensionless entanglement number

$$Z = \frac{M_w}{M_e}, \qquad (2)$$

where M_w is the mass-averaged molecular weight of the melt and the entanglement molecular weight, M_e, is determined from linear rheology as shown later. It has been suggested that flow can disentangle a melt, thus reducing Z [18, 26]. This effect is discussed in Sec.5.2.

After deposition, any flow-induced deformation of the polymer begins to relax in the absence of flow gradients. Now the deposited filament is exposed to the surrounding air and begins to cool. The model assumes axisymmetric cooling of the filament to some ambient temperature T_a according to a prescribed boundary condition at the filament surface. The boundary condition is defined by some prescribed cooling rate β. The temperature decay couples to the constitutive model via the polymer relaxation times; since diffusion is arrested at solidification, τ_d and τ_R both diverge at the glass transition temperature T_g.

For amorphous materials, if the glass transition occurs before the polymer has time to fully relax to equilibrium, then the model predicts a degree of residual alignment. The polymer configuration is characterised by tensor

$$\mathbf{A} = \frac{<\mathbf{RR}>}{2R_g}, \qquad (3)$$

where $\mathbf{R}$ is the end-to-end vector of the polymer chain and R_g is the polymers radius of gyration. The trace of

$\mathbf{A}$ defines the stretch of the polymer chain and the off-diagonal elements of $\mathbf{A}$ define the polymer's orientation. At equilibrium $\mathbf{A} = \mathbf{I}$. In a polar coordinate system, A_{rs} denotes alignment of the polymer in the flow direction. (Note that $\hat{\mathbf{r}}$ is directed out from the centre of the filament, and $\hat{\mathbf{s}}$ is directed in the direction of the flow.) Since A_{rs} evolves over time, we denote the time to reach the glass transition t_g and the residual alignment that locked in at the glass transition is denoted

$$A_{rs}(t = t_g) = \bar{A}. \qquad (4)$$

Determining the temperature dependence of the polymer relaxation times, as discussed in the next section, is key to calculating residual alignment. It is also clear that the molecular weight, or Z (Eq.2), plays a crucial role in the presence of residual stresses.

3.2. Rheology Characterization

The model relies on only three parameters to predict the non-linear flow behaviour of the melt. That is,

1. the elastic plateau modulus, G_e,
2. the entanglement molecular weight, M_e, and
3. the relaxation time of a polymer chain segment between entanglements, τ_e.

These three parameters can be determined from linear viscoelasticity measurements as follows. The values of the parameters are given in Table 2.

Shift factors obtained from time-temperature superposition of the storage and loss moduli, G' and G'', respectively, are assumed to take the form of the Williams-Landel-Ferry (WLF) equation

$$a(T) = \exp\left(-\frac{C_1(T - T_0)}{C_2 + T - T_0}\right), \qquad (5)$$

where T_0 is the reference temperature, and C_1, C_2 are constants. This shift factor governs how τ_d and τ_R diverge near to the glass transition; thus it is not necessary to explicitly define T_g in the model.

Then, the linear rheology master curve (G', G'' at T_0) is fit to the Likhtman-McLeish theory [27] using RepTate
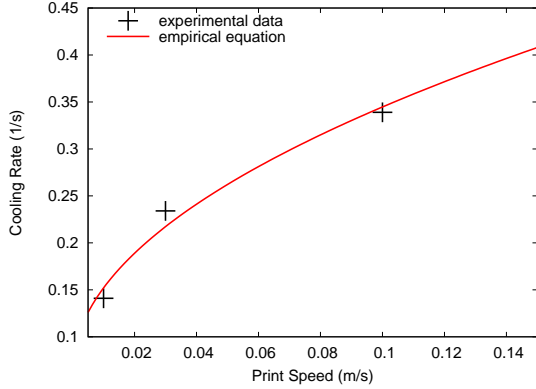
4

Figure 2: Experimentally measured (using infra-red imaging [22]) cooling rate of a deposited PLA filament of similar dimensions as a function of transverse print speed U_P. The data is fit to the functional form given in Eq.10, used to represent convective cooling. We find that $b_1 = 0.39$ s^{-1}, $b_2 = 5.28$ sm^{-1} and $b_3 = 0.06$ s^{-1}.
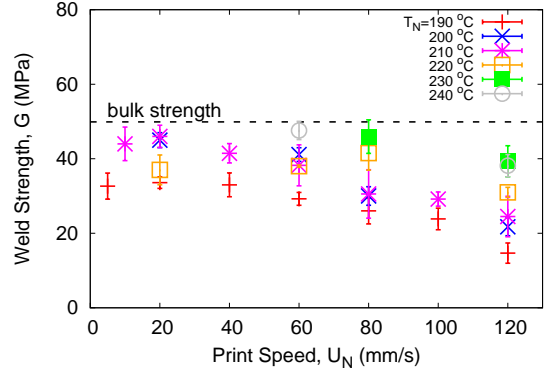

Figure 3: Weld fracture toughness measured using uniaxial tensile test (ASTMD1938) as a function of print speed, U_N, for a range of nozzle temperatures, T_N. Weld strength decreases with increased print speed and reduced nozzle temperatures.

software [28] to obtain G_e, M_e, and the entanglement time at the reference temperature, denoted τ_e^0 (See Appendix C). Note that the predicted M_e is in line with that reported in the literature [29]. The entanglement molecular weight is then used to determine the entanglement number, Z, via Eq.2. Once the entanglement time scale is established, the temperature-dependence of the reptation and Rouse times is given by

$$\tau_R = Z^2 \tau_e^0 a(T), \tag{6}$$

$$\tau_d = 3Z^3 \tau_e^0 \left(1 - \frac{3.38}{\sqrt{Z}} + \frac{4.17}{Z} - \frac{1.55}{\sqrt{Z}^3}\right) a(T), \tag{7}$$

where $a(T)$ is given by Eq.5.

3.3. Temperature Modelling

Axisymmetric cooling of the deposited filament is determined by solving heat equation:

$$\frac{\partial T}{\partial t} = \alpha \frac{1}{r} \frac{\partial}{\partial r} \left(r \frac{\partial T}{\partial r}\right), \tag{8}$$

for thermal diffusivity α. The initial condition is $T = T_N$ (i.e. we assume the temperature remains uniform during the nozzle and deposition flow). We prescribe the boundary condition at the filament surface to be

$$T_s(t) = \frac{(T_N - T_a)}{2} \exp(-\beta t) + T_a, \tag{9}$$

for some cooling rate β. This approach has been applied in previous works [10, 21, 22], and shows quantitative agreement with infra-red imaging measurements. Note that when the filament first touches the build plate, the temperature at the filament surface is assumed to be the average of the nozzle and bed temperature i.e. $T_s(t = 0) = (T_N + T_a)/2$.

We find empirically (Fig.2) that the cooling rate is related to the transverse velocity according to

$$\beta = b_1 \sqrt{b_2 U_P} + b_3, \tag{10}$$

for some constants b_1, b_2, b_3. This is the expected functional form for convection-driven cooling [30]; faster print speeds increase convection and therefore have a faster cooling rate.

4. Results

Here we demonstrate how increased print speed reduces the weld strength at filament-filament interfaces, as measured via the uniaxial tensile test described in Sec.2.3. We attribute this reduced strength to residual alignment, denoted $\bar{A}$ (Eq.4). We present our observations of residual alignment within a printed wall of PLA, as measured using the birefringence technique discussed in Sec.2.4, alongside the predictions from our MatEx model (Sec.3). Further details of the correlation between weld strength and residual alignment are deferred to the Sec.5.

4.1. Reduced weld strength

Fig.3 demonstrates that the weld strength is less than the bulk strength of the material for all printing conditions. Moreover, there is a clear reduction in the weld strength as a function of print speed, and that weld strength can be improved by increasing the nozzle temperature. Not only does increasing the temperature give more time above the glass transition temperature, it enables the polymers to relax faster. Thus, it is expected that filaments printed at higher temperatures are more isotropic and consequently have stronger welds. Birefringence measurements enable us to explore this hypothesis experimentally.

4.2. Observations of residual alignment

Fig.4 shows a polarised optical microscopy image of a single-filament printed wall; the image focuses on 5 filaments. Bright regions correspond to filament-filament interfaces and indicate that the polymer is oriented near to the welds. On the other hand, dark regions in the centre of each filament indicate that the polymer is isotropic. There is a small difference in the width of the oriented
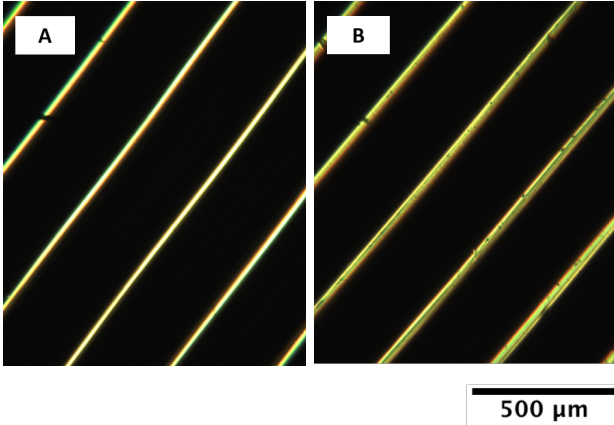
5

Figure 4: POM micrograph, under crossed polarizers of several printed filaments for (a) $T_N = 240°C$, $U_N = 120$ mm/s and (b) $T_N = 190°C$, $U_N = 120$ mm/s. Bright regions indicate polymer orientation, and correspond to filament-filament interfaces, whereas dark regions indicate isotropy at the centre of the printed filaments.

Figure 5: Apparent degree of birefringence in the weld as a function of print speed, U_N, for a range of different nozzle temperatures, T_N. Increased birefringence corresponds to an increase in residual alignment at fast print speeds and low nozzle temperatures.

region, with the lower-temperature case showing a wider birefringent area.

Fig.5 shows the degree of apparent birefringence for a range of printing conditions. At low nozzle temperatures ($T_N = 190 - 210°C$), the apparent birefringence increases linearly with print speed. For higher nozzle temperatures, lower apparent birefringence values are obtained and there is little dependence on print speed. Since birefringence traces molecular orientation, it is evident that anisotropy persists in the weld region.

To verify that the observed birefringence is related to the presence of amorphous oriented chains, rather than crystal fractions, calorimetric analysis was carried out on the printed samples to determine the sample crystallinity (see Appendix A). These tests show the presence of approximately 2-3% crystal phase by weight, over the total quantity of material, which may possibly be induced by the flow [21, 22]. However, by comparing the thickness of the birefringent region with respect to the filament, we find that the oriented region typically represents more than 12% of the total thickness (unlike the 2-3% of the crystallinity identified at the DSC). Furthermore, we observe similar birefringence with PETG - a non-crystalline polymer (see Appendix D).

Next, we employ our numerical model to investigate the mechanism leading to residual alignment only at the weld interfaces.

4.3. Model Predictions

Fig.6 shows the predicted residual alignment locked in the glass transition within a filament cross-section, as predicted by our numerical model. We show results for two print speeds, $U_N = 20$ and 120 mm/s, at nozzle temperature $T_N = 190$ °C. Although the polymers at the centre of the filament are isotropic at solidification, there is insufficient time for polymers near to the filament surface to
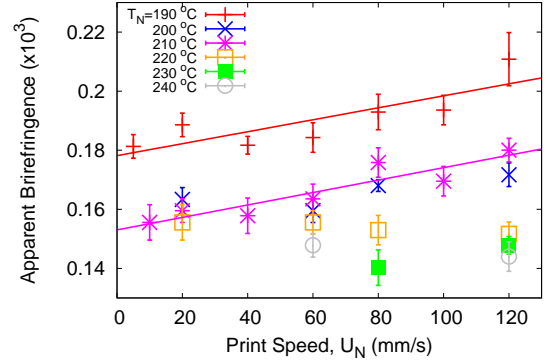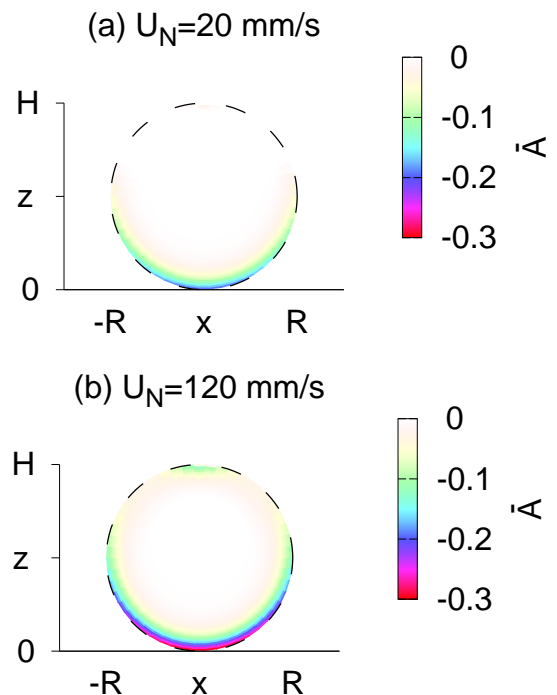

Figure 6: Degree of residual alignment, A_{rs} locked in at the glass transition over the cross-section of a deposited filament printed $T_N = 200°C$ for print speed (a) $U_N = 20$ mm/s and (b) $U_N = 120$ mm/s. The model predicts that the residual stress is localized in a thin boundary region near to the filament surface and increases with print speed.

relax to equilibrium before the onset of the glass transition. Thus, we observe a thin boundary layer of residual alignment, which is more prevalent at the bottom of the filament (due to the 90 degree turn during deposition [17]). Moreover, a larger degree of alignment can be seen for the faster print speed. This is in agreement with the birefringence results shown in Fig.4.

Since we are interested in how this anisotropy affects welding, next we present how this alignment evolves during cooling within in the weld region, defined to be at $z = 0$. Fig.7 shows the evolution of the temperature, the polymer
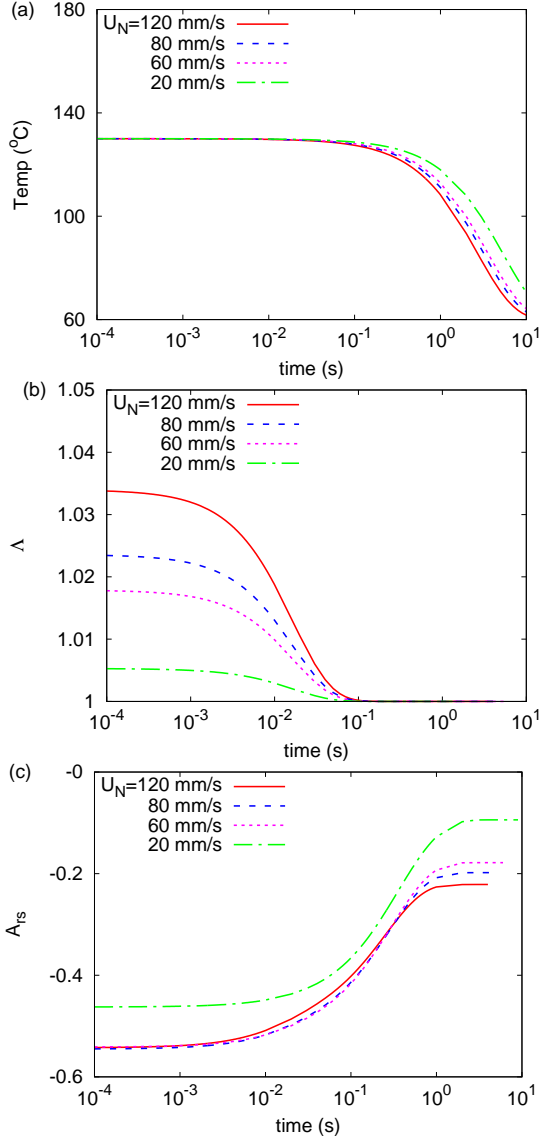
6

Figure 7: Evolution of (a) temperature, (b) the polymer stretch, $\Lambda = \sqrt{\mathrm{tr}\mathbf{A}/3}$, and (c) the orientation component, A_{rs}, at the weld ($z = 0$) predicted by the numerical model for increasing print speed at fixed nozzle temperature $T_N = 200°$C.
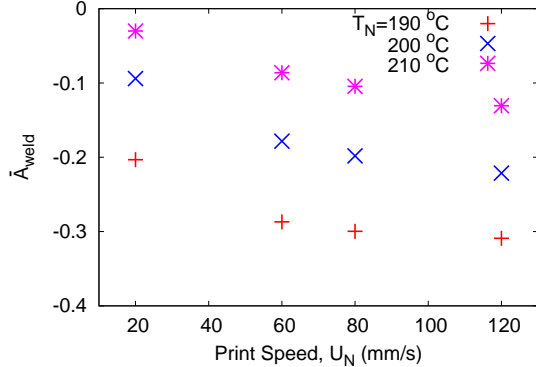

Figure 8: Final degree of alignment, $\bar{A}$, in the weld region (at $z = 0$) locked in the glass transition as a function of print speed for various nozzle temperatures.

stretch $\Lambda = \sqrt{\mathrm{tr}\mathbf{A}/3}$, and the alignment A_{rs}. First we note how filaments printed at faster speeds cool faster due to the imposed boundary condition (Eq.10), which represents increased convection for faster print speed.

Next, we note how faster printing imposes a greater initial polymer stretch and degree of alignment. Stretch relaxes on the order of the Rouse time (Eq.7), and has sufficient time to equilibrate before the glass transition. However, reptation is much slower and reorientation of the polymers is arrested by the glass transition, even for the slowest print speed, leading to residual alignment in the weld region. It is clear that the increased residual alignment with print speed is due to two factors:

1. a greater initial degree of alignment during flow through the nozzle and deposition, and
2. faster cooling leading to less time above the glass transition temperature.

Fig.8 shows the final degree of alignment $\bar{A}$ at the weld as function of print speed for three nozzle temperatures $T_N = 190, 200$ and 210 °C. The trends we observe with respect to the print conditions are evidently similar to those we report in terms of weld strength (Fig.3) and birefringence (Fig.5). That is, there is an increase in $|\bar{A}|$ and the degree of birefringence with increased print speed suggesting that increased residual anisotropy reduces weld strength; this effect can be reduced by increasing the nozzle temperature.

5. Discussion

Here we discuss the correlation between $\bar{A}$ and the experimentally measured apparent birefringence and weld strength. We also discuss additional factors, namely the inter-diffusion depth and entanglement fraction, which may also contribute to a reduced weld strength.

5.1. Alignment vs strength

Fig.9 clearly shows a linear relationship between $\bar{A}$ and the degree of apparent birefringence, Δn, in general agreement with the stress optical rule; we find that the shear stress $\sigma = G_e \bar{A}$ is related to the degree of apparent birefringence via

$$\Delta n \propto C_0 |\sigma|, \tag{11}$$

where $C_0 \approx 0.3$ GPa^{-1}. This is lower than the stress optical coefficient reported in the literature for PLA films [31, 32]. However, discrepancies may be expected due to relating the measured apparent birefringence for this 3D-printed wall geometry to the actual birefringence value at the weld.

Furthermore, the degree of birefringence is shown to reduce weld strength linearly. This suggests that even a small degree of residual alignment will reduce the strength at the weld, which we can predict via this empirical relation. These correlations between $\bar{A}$, the degree of birefringence and the weld strength form a basis for developing
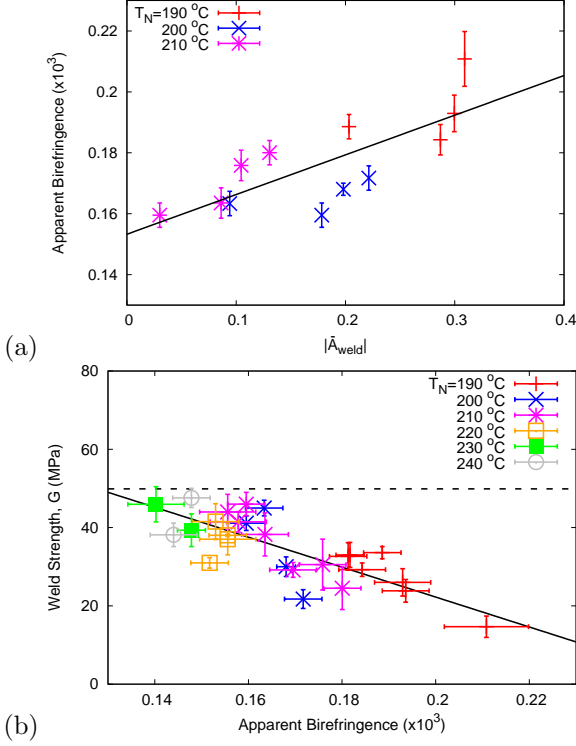
Figure 9: (a) The degree of apparent birefringence measured experimentally, δn, plotted against the final degree of alignment, $\bar{A}$, in the weld region predicted by the model (as in Fig.8). The line of best fit is linear. (b) Experimentally measured weld strength, G (as in Fig.3), as a function of the degree of apparent birefringence (as in Fig.5). Line shows linear line of best fit. Bulk strength is approximately 52 MPa.
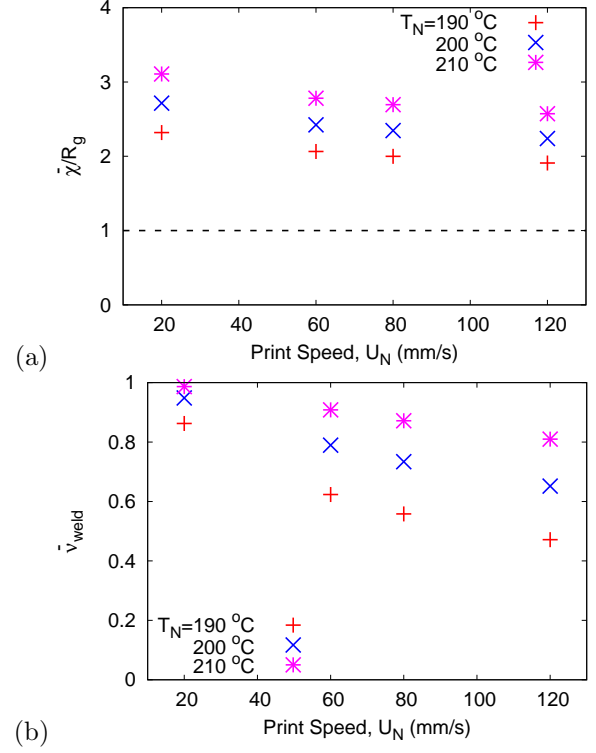
Figure 10: (a) Final interpenetration depth, $\bar{\chi}/R_g$, as estimated by Eq.12 at solidification as a function of print speed for various nozzle temperatures. Bulk strength is expected for $\bar{\chi}/R_g > 1$. (b) Final degree of entanglement, $\bar{\nu}$, predicted by the model in the weld region (at $z = 0$) at solidification,

more advanced theories to relate residual alignment to mechanical properties.

It is clear from our results that slower print speed and higher nozzle temperatures are favorable for preventing the entrapment of orientation at the glass transition. However, practically higher nozzle temperatures can lead to degradation, and slower print speeds reduce productivity. Thus, there is precedent for employing a post-printing thermal annealing process [33, 22] to remove these residual stresses. The appropriate annealing time and temperature can be chosen by inspection of the tube model parameters (Table 2), in particular the reptation time.

On the other hand, in some instances polymer alignment may be a desirable property for an FFF-printed part to tune electrical an mechanical properties. Furthermore, since PLA is a semi-crystalline polymer, thermal annealing under the correct conditions can also be employed to enhance crystallinity [22]; alignment from the printing flow leads to 'templated' flow-enhanced nuclei, which grow into smaller spherulite structures that exhibit more ductile fracture.

5.2. Interdiffusion and entanglements

Successful welding in MatEx is first and foremost reliant on diffusion of the polymer molecules across the filament-filament interfaces. This inter-diffusion process creates inter-facial entanglements, which increase the strength across the weld line [34]. Here we denote the final inter-penetration depth defined at the glass transition by $\bar{\chi}$. It is expected that if the polymer diffuses its radius of gyration during cooling, i.e. $\bar{\chi}/R_g > 1$, then bulk strength will be achieved in the weld region.

It has previously been shown that the inter-penetration depth can be approximated by [10]

$$\frac{\bar{\chi}}{R_g} = \left(36 \int_0^{t_g} \frac{1}{\tau_d(T(t))} \left(1 - (A_{rr}(t) - 1) \right) \right)^{1/4}. \quad (12)$$

The term containing A_{rr} accounts for anisotropic diffusion due to alignment in the flow direction in the weld region ($z = 0$).

Fig.10(a) shows the model predictions for $\bar{\chi}$ as a function of print speed and temperature (see Appendix F for details of $\chi(t)$). We see that for this material, and the range of print conditions considered here, there is always sufficient time prior to the glass transition to achieve adequate diffusion. Similar behaviour has also been predicted for polycarbonate [10]. Thus, we propose that reduced weld strength is not due to insufficient diffusion depths, but to the configuration of the entanglement network itself. Indeed, as described in the introduction, generally fracture of glassy polymers is governed by the number of 'interfacial' entanglements that act to anchor chains across the tear [14].

8

Here we consider the recently proposed mechanism of flow-induced disentanglement of the network due to convective constraint release (CCR). In the tube model, CCR is the mechanism of neighbouring chains reptating away due to thermal motion and thereby "releasing a constraint". At equilibrium, chains that reptate away are readily replaced by new chains, thus the number of entanglements remains constant. On the other hand, under flow there is an argument for CCR leading to a reduction in the number of entanglements.

Our previous work (Ref.[10]) employed the model of Ianniruberto [18] to account for changes in the entanglement fraction, denoted ν, due to the flow field. MatEx printing flow is found to significantly disentangle the polymer network i.e $\nu \ll 1$. Moreover, there is insufficient time for entanglements to recover to equilibrium ($\nu = 1$) during typical cooling. This leads to a partially-entangled melt at solidification, which is expected to be weaker than the bulk material.

Fig.10(b) shows the predicted results when flow-induced disentanglement followed by recovery during cooling is incorporated for the PLA material and printing conditions considered here. In particular, we find that the entanglement fraction locked in at the glass transition $\bar{\nu}$ within the weld region ($z = 0$) decreases with increasing print speed and reduced nozzle temperature. Full details of the implementation of this model are given in Appendix E.

Having a prediction of the reduced entanglement fraction within a MatEx-printed weld, we refer to the molecular interpretation of the toughness of glassy polymers [35, 36]. Typically glassy polymers fail in the crazing regime, where the toughness is shown to vary with the density of entangled chains per unit of craze area. Since the failure we observe in this work is brittle (showing no large plastic deformation), we propose a similar mechanism for PLA. Future work will focus on confirming this via a morphological investigation into the failure mechanism of printed PLA.

Thus, we modify this classic result [35, 36] to account for a partially entangled network prior to fracture; the final degree of entanglement $\bar{\nu}$ at the weld can be related to the weld fracture toughness via

$$G \sim \left(1 - \frac{p}{q}\frac{1}{\bar{\nu}Z_{eq}}\right)^2 \tag{13}$$

where p is the polydispersity index. The factor q is a measure of the fraction of strands that survive fibrillation during a tear and is found to be $q \approx 0.6$ in Ref.[37]. This approach has been applied in previous work [10], but a comparison to experimental data in not made. Here Fig.11 shows the predicted weld fracture toughness for the conditions considered in this work (lines). These results are quantitatively similar to that measured experimentally (points).
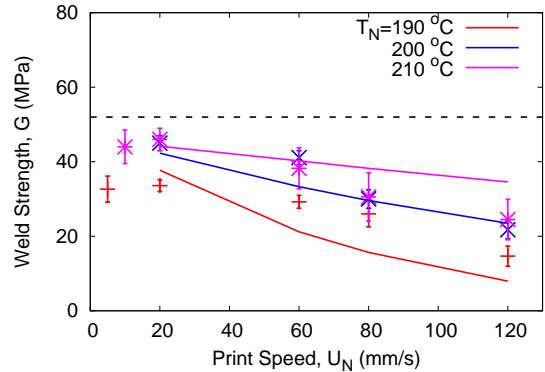

Figure 11: Weld fracture toughness, G as predicted by the model (Eq.13 with $q = 0.35$) *(lines)* and measured experimentally *(points)* as in Fig.3. Results are shown as a function of print speed for various nozzle temperatures. Bulk toughness is approximately 52 MPa.

6. Conclusion

For the first time, we have measured molecular orientation in a simple MatEx-printed object using birefringence. In particular, residual orientation of the polymer chains due to the printing flow is found to be localised to the weld regions between printed filaments. In contrast, the bulk of each filament is isotropic. There is a distinct decrease in weld strength with the increase of birefringence measured at the weld, which can be improved by increasing the nozzle temperature or reducing the print speed.

Our birefringence measurements can be directly linked to an alignment factor predicted by a molecularly-aware non-isothermal model of the MatEx process [10]. Our model confirms that polymer chains become oriented in the flow direction due to shear in the nozzle combined with the subsequent deposition process. Since the filament center experiences less severe velocity and temperature gradients, flow-induced deformation can fully relax prior to solidification. On the other hand, the filament surface is subject to greater shear and cooling rates and there is insufficient time for any flow-induced orientation to relax before the onset of the glass transition. We find that the predicted residual alignment factor at the weld, $\bar{A}$, is linearly proportional to the measured degree of apparent birefringence, Δn, in agreement with the stress-optical rule.

Furthermore, contrary to what is commonly expected, our model shows that weld strength is not limited by interdiffusion of the polymer molecules across filament-filament interfaces; instead weld strength is affected by the (non-equilibrium) configuration of the entanglement network itself. By relating the degree of residual alignment to partial entanglement of the polymer chains at solidification [38], we can predict the measured weld toughness via a modification to classic fracture theory of glassy polymers [35, 36]. Thus, this model may be used as a tool for choosing appropriate printing conditions based on a toughness threshold.

Interestingly, the trend of decreasing weld strength with increasing print speed is not apparent for ABS [8]. Unlike PLA, which can be characterised as a linear polymer and

obeys classic Doi-Edwards tube theory, ABS has a more complex microstructure that includes cross links and contains rubber nano-particles. Indeed, the rheology shown [8] is consistent with some very slow relaxing material in this sample. We'd expect this element of the material to behave affinely (or very close to this) under flow, leading to no dependence on the flow rate. The PLA material investigated here behaves very differently because its relaxation rates are comparable to the flow rates during printing. In future work, we will extend our analysis to other thermoplastic materials and consider the effect of molecular weight.

7. Acknowledgements

Appendix A. Differential Scanning Calorimetry

Using differential scanning calorimetry (DSC), we find that upon standard cooling at a rate of 10 °C/min, the material can barely crystallize (see Fig.A.12) and is almost totally amorphous, with a crystallinity index lower than 1%. Since the cooling rate in MatEx in generally much faster, it follows that the 3D-printed wall is amorphous.
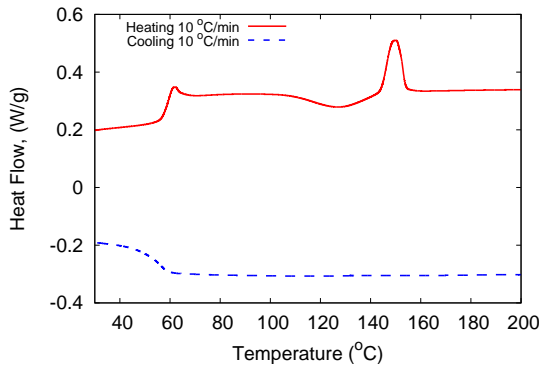
Figure A.12: DSC heating and cooling curve of the investigated PLA grade, measured at the rate of 10 °C/min

Appendix B. Measuring Weld Strength

An example micrograph from the weld width measurement technique described in Sec.2.3 is shown in Fig.B.13(a). A representative stress-strain curve is shown in Fig.B.13(b), demonstrating that the maximum stress and stress at break are equivalent in this case.
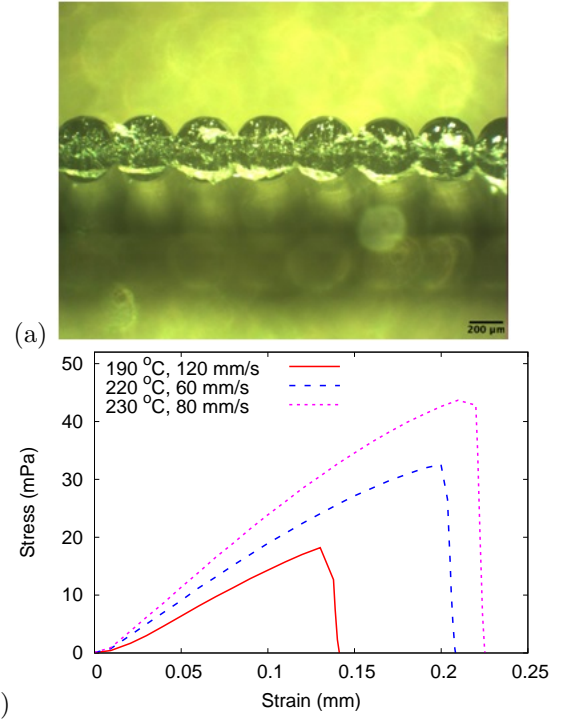
Figure B.13: (a) An example micrograph from the weld width measurement technique described in Sec.2.3. (b) Representative stress-strain curve.

Appendix C. Linear Viscoelasticity

PLA's linear viscoelastic properties are measured. The linear rheology master curve (G', G'' at T_0) is fit to the Likhtman-McLeish theory [27] using RepTate software [28], as shown in Fig. C.14 to obtain G_e, M_e, and the entanglement time at the reference temperature, denoted τ_e^0.
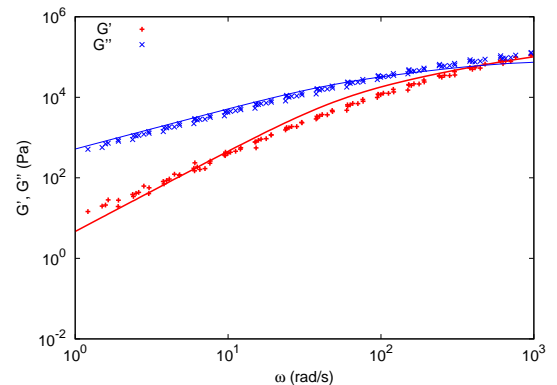
Figure C.14: Linear rheology master curve for PLA measured at reference temperature $T_0 = 200°$C *(points)* is fit to Likhtman-McLeish theory *(lines)*.

Appendix D. PETG

Fig.D.15 shows that we observe a similar phenonomen of birefringent weld regions in sample printed using PETG

- a non-crystalline polymer. This confirms that the birefringence arises from molecular orientation rather than crystalline domains.
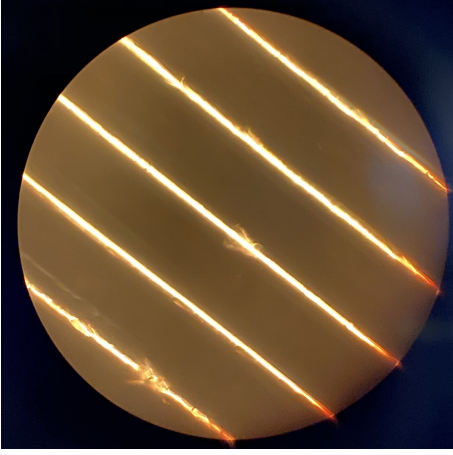

Figure D.15: POM micrograp under under crossed polarizers of several printed filaments of PETG. Bright regions indicate polymer orientation, and correspond to filament-filament interfaces, whereas dark regions indicate isotropy at the centre of the printed filaments.

Appendix E. Flow Modelling

Full details of the model derivation are given in [17]. Here we outline the key equations.   For pressure-driven flow through an axisymmetric nozzle that has reached steady state, the velocity profile is written as

$$\mathbf{u} = (0, 0, w(r)), \tag{E.1}$$

in polar coordinates, where s denotes the flow direction. The melt velocity is governed by conservation of momentum via

$$\frac{dp}{ds} = \frac{1}{r}\frac{\partial}{\partial r}\left(r\frac{\partial \sigma_{rs}}{\partial r}\right). \tag{E.2}$$

Here σ_{rs} denotes the shear stress. The pressure gradient dp/dz is constant and chosen to give a prescribed (radially-averaged) extrusion speed U_N. We assume no slip at the nozzle wall so that

$$w(r = R_N) = 0, \tag{E.3}$$

and the solution must be bounded at $r = 0$.

The residence time in the nozzle is given by $\tau_{res} = L_{noz}/U_N$, where $L_{noz} \approx 1$ mm is the length of the nozzle extruder section. Since $\tau_{res} \sim \tau_d \approx 0.008$ s at the hottest nozzle temperature $T_N = 240$ °C and fastest print speed $U_N = 120$ mm/s, the assumption of steady state flow is justified.

The shear stress is given by Newtonian and polymer contributions, such that

$$\sigma_{rs} = \mu_s \frac{\partial w}{\partial r} + G_e A_{rs}, \tag{E.4}$$

where μ_s is the solvent viscosity (arising from short chains in the melt), G_e is the plateau modulus, and A_{rs} describes the degree of polymer alignment.

In fact, A_{rs} is the only non-zero off-diagonal entry of the polymer configuration tensor $\mathbf{A}$. The trace of the configuration tensor determines the degree of polymer stretch, denoted

$$\Lambda = \sqrt{\frac{\mathrm{tr}\mathbf{A}}{3}}. \tag{E.5}$$

For the steady-state nozzle flow described above, according to the Rolie-Poly model the configuration tensor is given by

$$(\nabla\mathbf{u}\cdot\mathbf{A}) + (\mathbf{A}\cdot(\nabla\mathbf{u})^T) =$$
$$\frac{1}{\tau_d(T)}(\mathbf{A} - \mathbf{I}) + \frac{2}{\tau_R(T)}\left(1 - \frac{1}{\Lambda}\right)\left(\mathbf{A} + \frac{\beta_{CCR}}{\Lambda}(\mathbf{A} - \mathbf{I})\right), \tag{E.6}$$

and is coupled to conservation of momentum (Eq.E.2). The convective constraint release parameter β_{CCR} is set to 0.5 in this work to avoid shear banding instabilities in the nozzle. Eq.E.6 demonstrates that relaxation of the alignment is intimately linked to the stretch relaxation.

For flow through the nozzle, the entanglement fraction at steady state is determined by

$$\nu = \frac{1}{1 + \beta_{CCR}A_{rs}\frac{\partial w}{\partial r}\tau_d}. \tag{E.7}$$

For the deposition flow, the no-slip condition (Eq.E.3) is relaxed and the extrudate is assumed to instantly reach a uniform velocity upon exiting the nozzle. Since we prescribe the geometry of the corner region, the velocity profile is decoupled from the constitutive equation and given simply by conservation of mass (Eq.1). In general, during a fast deposition the polymer deformation is advected around the corner via

$$(\mathbf{u}\cdot\nabla)\mathbf{A} = (\nabla\mathbf{u}\cdot\mathbf{A}) + (\mathbf{A}\cdot(\nabla\mathbf{u})^T)$$
$$- \frac{1}{\tau_d(T)}(\mathbf{A} - \mathbf{I}) - \frac{2}{\tau_R(T)}\left(1 - \frac{1}{\Lambda}\right)\left(\mathbf{A} + \frac{\beta_{CCR}}{\Lambda}(\mathbf{A} - \mathbf{I})\right), \tag{E.8}$$

allowing for melt relaxation. Similarly, the entanglement fraction is advected via

$$(\mathbf{u}\cdot\nabla)\nu = -\beta_{CCR}((\mathbf{K}:\mathbf{A}) - (\mathbf{u}\cdot\nabla)\mathrm{tr}\mathbf{A})\nu + \frac{1-\nu}{\tau_d}. \tag{E.9}$$

We refer the reader to Ref.[17] for further details of this derivation.

Following deposition the melt relaxes via Rolie-Poly dynamics

$$\frac{d\mathbf{A}}{dt} = -\frac{1}{\tau_d(T)}(\mathbf{A}-\mathbf{I}) - \frac{2}{\tau_R(T)}\left(1 - \frac{1}{\Lambda}\right)\left(\mathbf{A} + \frac{\beta_{CCR}}{\Lambda}(\mathbf{A} - \mathbf{I})\right), \tag{E.10}$$

with an initial condition determined by the deposition flow. Similarly, entanglements recover via

$$\frac{d\nu}{dt} = \beta_{CCR}\nu\frac{d\mathrm{tr}\mathbf{A}}{dt} + \frac{1-\nu}{\tau_d}, \qquad \text{(E.11)}$$

again with an initial condition determined by the deposition flow.

Note that Ianniruberto's continuum-level model for disentanglement is in agreement with molecular dynamics simulations, as shown in Ref. [18]. One characteristic of this model is that during re-entanglement of the network, entanglements do not reform whilst the tube is stretched; as the tube stretch relaxes the polymer is retracting and therefore cannot gain entanglements during this time. However, molecular dynamics simulations do not demonstrate similar re-entanglement dynamics [39] (in contrast to the disentanglement behaviour).

Furthermore, in previous work [10, 18], the reptation time, τ_d, and thereby the Rolie-Poly equation, is dependent on ν, so that a partially entangled melt has a faster diffusion time and relaxes more quickly. However, this behaviour is in contrast to recent molecular dynamics simulations [40]. In light of this work, here we choose the reptation time, τ_d, to be dependent on temperature *only*, so that the Rolie-Poly equation is independent of ν. Thus, there is only a one-way coupling of the entanglement dynamics to the configuration dynamics.

In this way, ν can be thought of as an additional representation of the degree of alignment given by $\mathbf{A}$ (rather than a description of an evolving tube diameter). Indeed, we propose that ν can be considered as a measure of how well 'braided' the network is (rather than intimately linked to the tube dynamics), and thus can be related to the weld strength, as shown in the main text.

Appendix F. Evolution of χ and ν

For completeness, Fig.F.16 shows the evolution of the interpenetration depth χ and the entanglement fraction ν during cooling. We present the results for four different print speeds, and fixed nozzle temperature $T_N = 200$ °C. Diffusion is arrested once the glass transition temperature is reached at time $t = t_g$. Thus, t_g determines the final interpenetration depth as shown in Fig.10 and the final entanglement fraction as shown in Fig.11. Here we can also see the delay in entanglement recovery due to stretch relaxation (compare to Fig.7(b).)

Figure F.16: Evolution of the (a) diffusion depth, χ, and (b) the entanglement fraction ν predicted by the numerical model for increasing print speed at fixed nozzle temperature $T_N = 200$°C.

References

[1] A. Ambrosi, M. Pumera, 3d-printing technologies for electrochemical applications, Chemical Society Reviews 45 (2016) 2740–2755.

[2] E. Fuenmayor, C. O'Donnell, N. Gately, P. Doran, D. M. Devine, J. G. Lyons, C. McConville, I. Major, Mass-customization of oral tablets via the combination of 3d printing and injection molding, International journal of pharmaceutics 569 (2019) 118611.
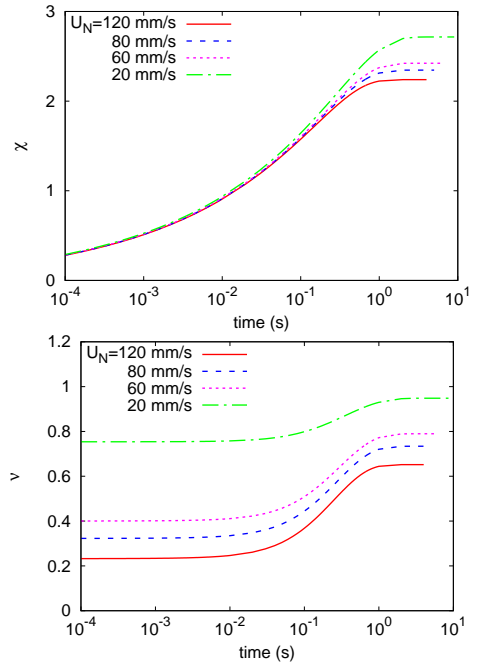
[3] S. Portanguen, P. Tournayre, J. Sicard, T. Astruc, P.-S. Mirade, Toward the design of functional foods and biobased products by 3d printing: A review, Trends in food science & technology (2019).

[4] J. M. Jordan, Additive manufacturing ("3d printing") and the future of organizational design: some early notes from the field, Journal of Organization Design 8 (2019) 5.

[5] J.-C. Wang, H. Dommati, J. Cheng, A turnkey manufacturing solution for customized insoles using material extrusion process, in: 3D Printing and Additive Manufacturing Technologies, Springer, 2019, pp. 203–216.

[6] G. Goh, Y. Yap, H. Tan, S. Sing, G. Goh, W. Yeong, Process–structure–properties in polymer additive manufacturing via material extrusion: A review, Critical Reviews in Solid State and Materials Sciences (2019) 1–21.

[7] M. Harris, J. Potgieter, R. Archer, K. M. Arif, Effect of material and process specific factors on the strength of printed parts in fused filament fabrication: a review of recent developments, Materials 12 (2019) 1664.

[8] J. E. Seppala, S. H. Han, K. E. Hillgartner, C. S. Davis, K. B. Migler, Weld formation during material extrusion additive manufacturing, Soft Matter 13 (2017) 6761–6769.

[9] D. Croccolo, M. De Agostinis, G. Olmi, Experimental characterization and analytical modelling of the mechanical behaviour of fused deposition processed parts made of ABS-M30, Computational Materials Science 79 (2013) 506–518.

[10] C. McIlroy, P. D. Olmsted, Disentanglement effects on welding behaviour of polymer melts during the fused-filament-fabrication method for additive manufacturi, Polymer 123 (2017) 376–391.

[11] L. Broutman, F. McGarry, Fracture surface work measurements on glassy polymers by a cleavage technique. ii. effects of crosslinking and preorientation, Journal of Applied Polymer Science 9 (1965) 609–626.

[12] J. Curtis, The effect of pre-orientation on the fracture properties of glassy polymers, Journal of Physics D: Applied Physics 3 (1970) 1413.

[13] K. Gotham, I. Scrutton, Effect of molecular orientation on the fracture toughness of thermoplastics, Polymer 19 (1978) 341–

347.

[14] H.-H. Kausch, Polymers/properties and applications. vol. 2. polymer fracture., Springer-Verlag, (1987) 456.

[15] J. Embery, R. Graham, R. Duckett, D. Groves, M. Collis, M. Mackley, T. McLeish, Tearing energy study of "oriented and relaxed" polystyrene in the glassy state, Journal of Polymer Science Part B: Polymer Physics 45 (2007) 377–394.

[16] M. Galvani, M. Robbins, Effect of chain alignment and entanglements on thermal welding in fused filament fabrication, Bulletin of the American Physical Society (2020).

[17] C. McIlroy, P. D. Olmsted, Deformation of an amorphous polymer during the fused-filament-fabrication method for additive manufacturing, Journal of Rheology 61 (2017) 379–397.

[18] G. Ianniruberto, G. Marrucci, Convective constraint release (CCR) revisited, Journal of Rheology 58 (2014) 89–102.

[19] M. Jin, R. Giesa, C. Neuber, H.-W. Schmidt, Filament materials screening for fdm 3d printing by means of injection-molded short rods, Macromolecular Materials and Engineering 303 (2018) 1800507.

[20] R. A. Auras, L.-T. Lim, S. E. Selke, H. Tsuji, Poly (lactic acid): synthesis, structures, properties, processing, and applications, volume 10, John Wiley & Sons, 2011.

[21] C. McIlroy, R. Graham, Modelling flow-enhanced crystallisation during fused filament fabrication of semi-crystalline polymer melts, Additive Manufacturing 24 (2018) 323–340.

[22] J. E. Seppala, A. P. Kotula, C. R. Snyder, Polymer-Based Additive Manufacturing: Recent Developments. ACS Symposium Series, American Chemical Society, Washington, DC, 2019.

[23] Web address:, https://www.makeitfrom.com/material-properties/Polylactic-Acid-PLA- Polylactide, 2019.

[24] A. E. Likhtman, R. S. Graham, Simple constitutive equation for linear polymer melts derived from molecular theory: Rolie–Poly equation, Journal of Non-Newtonian Fluid Mechanics 114 (2003) 1–12.

[25] M. Doi, S. F. Edwards, The theory of polymer dynamics, Oxford University Press, Oxford, 1988.

[26] C. Baig, V. G. Mavrantzas, M. Kroger, Flow effects on melt structure and entanglement network of linear polymers: Results from a nonequilibrium molecular dynamics simulation study of a polyethylene melt in steady shear, Macromolecules 43 (2010) 6886–6902.

[27] A. E. Likhtman, T. C. McLeish, Quantitative theory for linear dynamics of linear entangled polymers, Macromolecules 35 (2002) 6332–6343.

[28] A. Likhtman, Reptate, https://reptate.readthedocs.io/, 2019.

[29] J. R. Dorgan, J. S. Williams, D. N. Lewis, Melt rheology of poly (lactic acid): Entanglement and chain architecture effects, Journal of rheology 43 (1999) 1141–1155.

[30] G. Lamberti, G. Titomanlio, V. Brucato, Measurement and modelling of the film casting process 1. width distribution along draw direction, Chemical Engineering Science 56 (2001) 5749–5761.

[31] J. Mulligan, M. Cakmak, Nonlinear mechanooptical behavior of uniaxially stretched poly (lactic acid): Dynamic phase behavior, Macromolecules 38 (2005) 2333–2344.

[32] X. Ou, Structural mechanisms as revealed by real time mechano optical behavior of polylactic acid films in uni and biaxial deformation and heat setting processes, The University of Akron, 2004.

[33] J. Torres, J. Cotelo, J. Karl, A. P. Gordon, Mechanical property optimization of fdm pla in shear with multiple objectives, Jom 67 (2015) 1183–1193.

[34] T. Ge, F. Pierce, D. Perahia, G. S. Grest, M. O. Robbins, Molecular dynamics simulations of polymer welding: Strength from interfacial entanglements, Physical review letters 110 (2013) 098301.

[35] E. J. Kramer, P. Green, C. J. Palmstrøm, Interdiffusion and marker movements in concentrated polymer-polymer diffusion couples, polymer 25 (1984) 473–480.

[36] H. Brown, A molecular interpretation of the toughness of glassy polymers, Macromolecules 24 (1991) 2752–2756.

[37] Y. Sha, C. Hui, A. Ruina, E. Kramer, et al., Continuum and discrete modeling of craze failure at a crack-tip in a glassy polymer, Macromolecules 28 (1995) 2450–2459.

[38] G. Ianniruberto, Quantitative appraisal of a new ccr model for entangled linear polymers, Journal of Rheology 59 (2015) 211–235.

[39] T. O'Connor, private communication, 2019.

[40] T. C. O'Connor, A. Hopkins, M. O. Robbins, Stress relaxation in highly oriented melts of entangled polymers, Macromolecules (2019).

13